Article type : Original Paper

# INCREASED TRANSPORT OF ACETYL-COA INTO THE ENDOPLASMIC RETICULUM CAUSES A PROGERIA-LIKE PHENOTYPE

Yajing Peng [1,2], Samantha L. Shapiro [1,2], Varuna C. Banduseela [1,2,†], Inca A. Dieterich [1,2,3], Kyle J. Hewitt [4], Emery H. Bresnick [4], Guangyao Kong [4], Jing Zhang [4], Kathryn L. Schueler [5], Mark P. Keller [5], Alan D. Attie [5], Timothy A. Hacker [6], Ruth Sullivan [7], Elle Kielar-Grevstad [5], Sebastian I. Arriola Apelo [1,‡], Dudley W. Lamming [1], Rozalyn M. Anderson [1,9], and Luigi Puglielli [1,2,8,9,*]

[1]Department of Medicine, University of Wisconsin-Madison, Madison, WI 53705, USA

[2]Waisman Center, University of Wisconsin-Madison, Madison, WI 53705, USA

[3]Neuroscience Training Program, University of Wisconsin-Madison, Madison, WI 53705, USA

[4]Department of Cell and Regenerative Biology, University of Wisconsin-Madison, Madison, WI 53705, USA

[5]Department of Biochemistry, University of Wisconsin-Madison, Madison, WI 53705, USA

[6]Cardiovascular Research Center, University of Wisconsin-Madison, Madison, WI 53705, USA

[7]Department of Comparative Biosciences, University of Wisconsin-Madison, Madison, WI 53705, USA

[8]Department of Neuroscience, University of Wisconsin-Madison, Madison, WI 53705, USA

[9]Geriatric Research Education Clinical Center, Veterans Affairs Medical Center, Madison, WI 53705, USA

**FOOTNOTES:**

[†]Current affiliation: Department of Internal Medicine, University of Michigan, Ann Arbor, MI, USA

[‡]Current affiliation: Department of Dairy Science, University of Wisconsin-Madison, Madison, WI, USA

***Correspondence**:
Luigi Puglielli, University of Wisconsin-Madison, Waisman Center, 1500 Highland Ave, Madison, WI 53705, USA. E-mail: lp1@medicine.wisc.edu

**Running Title:** AT-1, reticulophagy and progeria

**Keywords:** Acetyl-CoA; AT-1/SLC33A1; progeria; ATase1; ATase2; lysine acetylation

**CHECKLIST**

**Total character count:** 48,543 (including spaces)

**Word count of the Summary:** 240

**Number of papers cited in the References:** 53

**List of Tables:** Table 1

**List of Figures:** Fig. 1 (color), Fig. 2 (color), Fig. 3 (color), Fig. 4 (color), Fig. 5 (color), Fig. 6 (greyscale), Fig. 7 (color).

**Supplemental Figures:** 8

**SUMMARY**

The membrane transporter AT-1/SLC33A1 translocates cytosolic acetyl-CoA into the lumen of the endoplasmic reticulum (ER), participating in quality control mechanisms within the secretory pathway. Mutations and duplication events in *AT-1/SLC33A1* are highly pleiotropic and have been linked to diseases such as spastic paraplegia, developmental delay, autism spectrum disorder, intellectual disability, propensity to seizures, and dysmorphism. Despite these known associations, the biology of this key transporter is only beginning to be uncovered. Here, we show that systemic overexpression of AT-1 in the mouse leads to a segmental form of progeria with dysmorphism and metabolic alterations. The phenotype includes delayed growth, short lifespan, alopecia, skin lesions, rectal prolapse, osteoporosis, cardiomegaly, muscle atrophy, reduced fertility, and anemia. In terms of homeostasis, the AT-1 overexpressing mouse displays hypocholesterolemia, altered glycaemia, and increased indices of systemic inflammation. Mechanistically, the phenotype is caused by a block in Atg9a-Fam134b-LC3β and Atg9a-Sec62-LC3β interactions, and defective reticulophagy, the autophagic recycling of the ER. Inhibition of ATase1/ATase2 acetyltransferase enzymes downstream of AT-1 restores reticulophagy and rescues the phenotype of the animals. These data suggest that inappropriately elevated acetyl-CoA flux into the ER directly induces defects in autophagy and recycling of subcellular structures and that this diversion of acetyl-CoA from cytosol to ER is causal in the progeria phenotype. Collectively, these data establish the cytosol-to-ER flux of acetyl-CoA as a novel event that dictates the pace of aging phenotypes and identify intracellular acetyl-CoA dependent homeostatic mechanisms linked to metabolism and inflammation.

## 1. INTRODUCTION

Nε-lysine acetylation in the lumen of the endoplasmic reticulum (ER) has emerged as a novel mechanism for the regulation of protein homeostasis (also referred to as proteostasis) within the organelle (Jonas *et al.* 2010; Pehar *et al.* 2012; Ding *et al.* 2014; Peng *et al.* 2014; Hullinger *et al.* 2016; Peng *et al.* 2016; Peng & Puglielli 2016). Acetylation of ER cargo proteins is ensured by three essential elements: AT-1, ATase1, and ATase2. AT-1 (also referred to as SLC33A1) is the ER membrane transporter that regulates the cytosol-to-ER flux of acetyl-CoA, donor of the acetyl group in the reaction of Nε-lysine acetylation (Jonas *et al.* 2010; Peng *et al.* 2014). ATase1 (also referred to as NAT8B) and ATase2 (also referred to as NAT8) are type II ER membrane proteins that carry out the reaction of Nε-lysine acetylation within the ER lumen (Ko & Puglielli 2009; Ding *et al.* 2014). *Ex vivo* and *in vivo* data suggest that the ER acetylation machinery is a component of ER quality control and regulates two essential functions of the organelle: (i) selection and transport of cargo proteins along the secretory pathway and (ii) disposal of protein aggregates that form within the ER and secretory pathway (Pehar *et al.* 2012; Ding *et al.* 2014; Peng *et al.* 2014; Hullinger *et al.* 2016; Peng *et al.* 2016; Peng & Puglielli 2016). The former requires the ATases to associate with the oligosaccharyl transferase complex (OST) and acetylate correctly folded polypeptides (Ding *et al.* 2014; Peng & Puglielli 2016) while the latter requires acetylation/deacetylation of the autophagy protein Atg9a (Pehar *et al.* 2012; Peng *et al.* 2014; Peng *et al.* 2016; Peng & Puglielli 2016). AT-1 regulates availability of acetyl-CoA within the ER; as such, it plays crucial regulatory functions for the entire ER acetylation machinery.

Clinically, diverse outcomes related to genetic deficiency, mutation, or overabundance of AT-1 have been identified. Children with homozygous mutations in *AT-1*/*SLC33A1* display congenital defects, severe developmental delay and premature death (Huppke *et al.* 2012; Chiplunkar *et al.* 2016). Patients with heterozygous mutations appear normal at birth but then develop a complicated autosomal dominant form of spastic paraplegia (Lin *et al.* 2008). Finally, chromosomal duplications of the 3q25.31 locus, which harbors *AT-1*/*SLC33A1*, have been reported in patients with autism spectrum disorder (ASD), intellectual disability, propensity to seizures, and facial dysmorphism (SFARI database; see also Swisshelm, K., et al. 2014. ASHG Annual Meeting; Abstract 3205T). The above disease phenotypes are mimicked by related mouse models. Knock-in mice that lack AT-1 activity (AT-$1^{S113R/S113R}$) die during embryogenesis, while mice with haploinsufficiency of AT-1 (AT-$1^{S113R/+}$) develop neurodegeneration with spasticity and propensity to infections and cancer (Peng *et al.* 2014). Transgenic mice that overexpress AT-1 in forebrain neurons (AT-1 Tg) display an ASD-like phenotype without dysmorphism (Hullinger *et al.* 2016). Mechanistically, the phenotype of AT-$1^{S113R/+}$ mice is linked to aberrant activation of autophagy (Peng *et al.* 2014) while the phenotype of AT-1 Tg is linked to increased efficiency of the

secretory pathway (Hullinger *et al.* 2016). When taken together, the convergence of human- and mouse-based studies clearly indicates that the ER acetylation machinery plays fundamental biological functions.

Despite these known associations, the biology of AT-1 and the ER acetylation machinery is only beginning to be uncovered. Here, we sought to investigate the broader consequences of AT-1 manipulation, including the cellular and systemic impact of AT-1 directed changes in ER acetylation, by generating a transgenic mouse where AT-1 was placed under the control of the Rosa26 locus. The animals developed a severe phenotype mimicking segmental forms of human progerias. At a mechanistic level, we observed increased acetylation of the ER-localized autophagy protein Atg9a, reduced Atg9a-Fam134b-LC3β and Atg9a-Sec62-LC3β interaction, and a block in ER-autophagy/reticulophagy. Finally, we showed that a specific ATase1/ATase2 inhibitor, which restores ER proteostatic functions downstream of AT-1, was able to rescue the entire phenotype of the animals, including the lifespan. Collectively, these data establish the cytosol-to-ER flux of acetyl-CoA as a novel event that dictates the pace of aging phenotypes and identify intracellular acetyl-CoA dependent homeostatic mechanisms linked to metabolism and inflammation.



## 2. RESULTS

### 2.1 AT-1 sTg mice display a progeria-like phenotype

To study the systemic role of AT-1, we generated transgenic (Tg) mice with an inducible overexpression Tet-Off system driven by the Rosa26 locus (**Figure 1a,b**). For the purpose of this study, the animals (referred to as AT-1 sTg) were maintained in the absence of doxycycline (Dox); therefore, they overexpressed AT-1 throughout their entire life, including development. The animals were born with Mendelian ratio and were completely normal at birth. However, within one month they appeared smaller than their wild-type/non-Tg (WT) littermates (**Figure 1c**), and within two months they displayed a severe phenotype (**Figure 1c**; **Table 1**) that was reminiscent of segmental forms of human progerias (Pivnick *et al.* 2000; Liao & Kennedy 2014; Gonzalo *et al.* 2017; Karikkineth *et al.* 2017). Indeed, they remained smaller throughout their entire lifespan (**Figure 1d**), appeared phenotypically old (**Figure 1c**), and displayed a very short lifespan (**Figure 1e**). The progeria-like features of the animals are listed in **Table 1**.

In addition to being small, AT-1 sTg mice were very thin and had small fat pads (**Figure 2a,b**); the significant reduction in fat tissue was observed despite the fact that they ate more than their WT littermates (**Figure 2c**). AT-1 sTg mice also displayed small areas of muscle atrophy (**Figure 2d**). However, relative to their body weight, they had overall enlarged organs (**Figure 2e**); the only exception was the uterus, which appeared significantly smaller and atrophic (**Figure 2e**; see ***Inset***). This finding is in line with the observed reduced fertility of female animals (**Table 1**). The skin displayed hair-loss, multiple lesions, and delayed wound repair (**Figure 1c; 2f; Table 1**). Histologically, we observed dermatitis with marked acanthosis and moderate orthokeratotic hyperkeratosis, reactive fibrosis, and epidermal hyperplasia (**Figure 2g**). Most of the animals also developed rectal prolapse (**Figure 2f**). Both male and female AT-1 sTg mice displayed severe bone density loss, which was reminiscent of human osteoporosis (**Figure 2h-j**). In line with the post-mortem data (**Figure 2e**), echocardiographic assessment of living animals confirmed that AT-1 sTg mice suffered from cardiomegaly very early in life (**Figure 2k,l**).

### 2.2 AT-1 sTg mice display defective hematopoiesis, metabolic alterations, and systemic inflammation

A complete blood count of AT-1 sTg mice revealed mild to moderate anemia, which was well evident in females (**Figure 3a**). The anemia was accompanied by splenomegaly and expansion of the spleen interfollicular/red pulp (extramedullary hematopoiesis) in both males and females (**Figure 3b**). We also observed reduced levels of circulating ferritin (**Figure S1a**) and iron (**Figure S1b**), increased reticulocyte ratio in the peripheral blood (**Figure 3c**), and reduced erythrocyte/nucleated ratio in the bone marrow (**Figure 3d**). Further assessment revealed a marked increase in erythroid progenitor activity in AT-1 sTg spleens relative to WT (**Figure 3e,f**). When taken together, the above results indicate that AT-1 overexpression disrupts steady-state hematopoiesis, causing splenomegaly and extramedullary erythropoiesis.

Metabolic assessment of AT-1 sTg mice revealed reduced levels of circulating glucose and insulin (**Figure 3g,h**) but normal levels of glucagon (**Figure S2a**). Lower levels of plasma glucose and insulin were also observed following an oral glucose tolerance test (**Figure 3i,j; S2b,c**) suggesting a more effective utilization of glucose. The metabolic assessment of the animals also revealed reduced levels of circulating cholesterol (**Figure 3k**).

Post-mortem examination of AT-1 sTg mice revealed enlarged lymph nodes (**Figure 4a**) as well as histological evidence for moderate inflammatory infiltration across different tissues and organs, indicative of systemic inflammation. Consistently, we observed increased levels of several inflammatory molecules in the plasma (**Figure 4b**) as well as a marked immunoglobulin infiltration of peripheral tissues (**Figure**

**4c-f**). The increased systemic inflammation in AT-1 sTg mice was also reflected in the significant increase in B cells and neutrophils in the peripheral blood relative to WT (**Figure 4g,h**). Chronic tissue inflammation is often associated with markers of cellular senescence (Tchkonia *et al.* 2013; Ovadya & Krizhanovsky 2014; Kang *et al.* 2015; Jeon *et al.* 2017). Therefore, we used isolated hepatocytes and liver sections to determine levels of p16, p21, and senescence-associated-β-galactosidase (SA-β-Gal), three established markers of cell senescence (Tchkonia *et al.* 2013; Ovadya & Krizhanovsky 2014; Kang *et al.* 2015; Jeon *et al.* 2017). We consistently found increased levels of the senescent markers in AT-1 sTg mice when compared to WT littermates (**Figure 4i-l**). These results were paralleled by a significant reduction in the proliferation potential of mouse embryonic fibroblasts (MEF) in culture (**Figure 4m,n**).

**2.3 AT-1 sTg mice display defective reticulophagy**

The above results indicate that systemic overexpression of AT-1 causes a complex phenotype that resembles human segmental progerias with metabolic alterations. We previously reported that the influx of acetyl-CoA from the cytosol to the ER lumen by AT-1 regulates the induction of ER-autophagy and the disposal of protein aggregates within the secretory pathway (Jonas *et al.* 2010; Pehar *et al.* 2012; Peng *et al.* 2014; Peng *et al.* 2016; Peng & Puglielli 2016). Therefore, it is possible that a defect in ER-autophagy (also referred to as reticulophagy) is at the basis of the progeria-like phenotype of AT-1 sTg mice.

To test the above hypothesis, we first analyzed the acetylation profile of the autophagy protein Atg9a, which is essential for the induction of autophagy downstream of the ER acetylation machinery (Pehar *et al.* 2012; Peng *et al.* 2014; Peng *et al.* 2016; Peng & Puglielli 2016). In fact, Atg9a undergoes acetylation on two lysine residues, K359 and K363, which face the lumen of the ER (Pehar *et al.* 2012). Acetylated Atg9a blocks the induction of autophagy while non-acetylated Atg9a exerts the opposite effect (Pehar *et al.* 2012). Direct assessment of ER membranes from WT and AT-1 sTg mice revealed a marked increase in the acetylation status of Atg9a in the transgenic animals (**Figure 5a,b**), thus supporting our hypothesis. To assess whether the increased acetylation of Atg9a was accompanied by reduced disposal of misfolded/aggregated ER cargo proteins, we took advantage of the pro-aggregating properties of the A53T mutant form of α-synuclein (A53T syn) (Polymeropoulos *et al.* 1997). Specifically, we used A53T syn with a signal peptide (SP) at the N-terminus to direct translation on the ER and insertion into the secretory pathway (Peng *et al.* 2016). The results show that when expressed in MEF, the levels of aggregated/SDS soluble SP-A53T syn were higher in AT-1 sTg vs WT animals (**Figure S3a,b**). This finding is consistent with previous data, where we showed a more efficient clearance of SP-A53T syn in MEF from AT-$1^{S113R/+}$ mice, which display reduced AT-1 activity, reduced acetylation of Atg9a, and increased induction of ER-autophagy (Peng *et al.* 2016). Therefore, when taken together, data from two

different animal models, AT-1 sTg (present study) and AT-1$^{S113R/+}$ (Peng *et al.* 2016) mice, as well as cellular systems (Pehar *et al.* 2012), support the conclusion that the increased acetylation of Atg9a in AT-1 sTg mice is causally linked to reduced ability of the ER to dispose of toxic protein aggregates that form within its lumen (see also later).

Previous data in MEF from AT-1$^{S113R/+}$ mice and H4 cells overexpressing AT-1 indicate that changes in autophagy induction down-stream of AT-1 are also paralleled by changes in efficiency of the secretory pathway; specifically, reduced AT-1 activity leads to reduced trafficking of newly synthesized glycoproteins along the secretory pathway while increased AT-1 activity leads to the opposite effect (Hullinger *et al.* 2016). To test whether this was indeed the case in AT-1 sTg mice, we used azide-modified mannosamine (ManNAz) to label sialic acid-containing newly-synthesized glycoproteins that have successfully trafficked from the ER to the *trans*-Golgi (Hullinger *et al.* 2016). The results show a significant increase in the levels of ManNAz incorporation in hepatocytes from AT-1 sTg animals (**Figure S3c**). Therefore, when taken together, the combined use of SP-A53T syn and ManNAz confirm the conclusion that changes in reticulophagy in AT-1 sTg mice are closely paralleled by opposite changes in the transport of cargo protein along the secretory pathway. These results are in line with previous data (Hullinger *et al.* 2016; Peng & Puglielli 2016).

In addition to reduced elimination of toxic protein aggregates, a significant block in reticulophagy is expected to cause structural reorganization of the organelle. To determine whether this was indeed the case, we used super-resolution microscopy, specifically structured illumination microscopy (SIM). Consistent with our prediction, we observed a profound reorganization of the ER in AT-1 sTg; particularly, we observed expansion of the organelle and enlarged sheet-like structures (**Figure 5c; S3d**). Even when comparing similar structures in WT and AT-1 sTg mice, the transgenic animals displayed a marked membrane proliferation with numerous processes emerging from the ER sheets (**Figure 5c**; discussed later).

### 2.4 AT-1 sTg mice display reduced Atg9a-Fam134b-LC3β and Atg9a-Sec62-LC3β interaction

The role of Atg9a as a potential "sensor" of the acetylation status of the ER has already been described (Pehar *et al.* 2012; Peng *et al.* 2014; Peng *et al.* 2016; Peng & Puglielli 2016). Thus, the above results are not surprising. However, what remains to be determined is how the acetylation of Atg9a on K359 and K363 within the lumen of the ER can activate the core of the autophagy machinery, which is mainly cytosolic (Klionsky *et al.* 2016). Interestingly, the above two lysine residues are flanked by two coiled regions that could be involved with protein-protein interactions (Pehar *et al.* 2012). This might suggest that the acetylation status of Atg9a regulates the interaction with other ER luminal or membrane-bound partners. However, since the core of the autophagy machinery is mainly cytosolic, a membrane-

bound protein is more likely to connect an ER-luminal event, acetylation of Atg9a, to the authophagy core machinery, specifically LC3β.

To address the above scenario and dissect the mechanism responsible for the block in reticulophagy, we studied levels and ER-association of Fam134b, a recently identified key regulator of reticulophagy (Khaminets *et al.* 2015; Mochida *et al.* 2015; Rubinsztein 2015). Interestingly, the ER expansion in AT-1 sTg mice was accompanied by a marked increase in the number of Fam134b puncta on the ER membrane (**Figure 5d,e**). The upregulation of Fam134b in AT-1 sTg mice was also observed when we analyzed mRNA (**Figure 5f**) and protein levels (**Figure 5g,h**). Fam134b has recently emerged as a novel regulator of ER-autophagy, and levels of Fam134b seem to reflect intrinsic dynamics of reticulophagy (Khaminets *et al.* 2015; Mochida *et al.* 2015; Nakatogawa & Mochida 2015; Rubinsztein 2015; Lennemann & Coyne 2017). Therefore, increased steady-state levels of Fam134b in AT-1 sTg mice (**Figure 5d-h**) are consistent with the observed ER expansion (**Figure 5c; S3d**), as they might reflect reduced turnover of the ER-associated Fam134b protein as well as an attempt of the cell to restore reticulophagy by activating Fam134b translation. Fam134b has a LC3-interacting region (LIR) on its C-terminus, which is required for binding to cytosolic LC3β (also referred to as Atg8 in yeast) (Khaminets *et al.* 2015; Mochida *et al.* 2015; Rubinsztein 2015). Fam134b-LC3β interaction is required for efficient induction of reticulophagy (Khaminets *et al.* 2015; Mochida *et al.* 2015; Rubinsztein 2015). Notably, despite the increased levels of Fam134b, we observed a marked reduction in Fam134b-LC3β co-localization in AT-1 sTg vs WT **(Figure 5i,j)**.

The finding that AT-1 sTg mice display less Fam134b-LC3β interaction led us to hypothesize that Atg9a, which acts as a sensor of ER acetylation (Pehar *et al.* 2012), might engage with Fam134b within the ER membrane. Indeed, immunoprecipitation of Atg9a from the ER membrane was able to pull-down Fam134b (**Figure 5k,l**); however, this interaction was markedly reduced in AT-1 sTg mice (**Figure 5k,l**) suggesting that the increased acetylation of Atg9a (**Figure 5a**) impedes functional interaction (see also later). The reduced Atg9a-Fam134b association in AT-1 sTg mice was observed despite the fact that we consistently pulled-down more Atg9a from the ER of the Tg animals compared to WT littermates (**Figure 5k**) and that Fam134b is upregulated in the Tg animals (**Figure 5g**; see also later).

Another important regulator of reticulophagy is Sec62, a member of the ER membrane translocon complex, which regulates import of newly synthesized proteins within the ER (Fumagalli *et al.* 2016). Like Fam134b, Sec62 also has a LIR domain, which is required for binding to LC3β; increased Sec62-LC3β interaction promotes reticulophagy and delivery of ER cargo proteins to autolysosomes (Fumagalli *et al.* 2016). As with Fam134b, SIM imaging revealed a marked reduction in Sec62-LC3β co-localization in AT-1 sTg vs WT animals **(Figure 5m,n)**. Furthermore, direct biochemical assessment revealed that Atg9a is able to engage Sec62 at the ER membrane; however, the Atg9a-Sec62 interaction was greatly

reduced in the AT-1 sTg mice **(Figure 5o,p)**. Again, this was observed even though we pulled down more Atg9a from the ER of the Tg animals (**Figure 5o**). SIM imaging showed that Fam134b-LC3β and Sec62-LC3β co-localization can be observed on the ER membrane (**Figure S3e**), suggesting that the initial interaction of Fam134b and Sec62 with LC3β can occur on the ER itself prior to the formation of the autophagosome. This process is blocked in AT-1 sTg mice (**Figure 5i-p**).

When taken together, the above results suggest that AT-1 overexpression and increased cytosol-to-ER flux of acetyl-CoA leads to increased acetylation of Atg9a and reduced Atg9a-Fam134b and Atg9a-Sec62 interaction within the ER membrane; this prevents interaction with LC3β thus causing a block in the induction of reticulophagy. Defective reticulophagy is then accompanied by expansion of the organelle. In essence, the acetylation status of Atg9a appears to regulate Fam134b-LC3β and Sec62-LC3β interaction and consequent induction of reticulophagy (also discussed later).

The insulin growth factor 1 (Igf-1) and its receptor (Igf-1r) (Longo & Finch 2003; Kenyon 2005; Milman *et al.* 2016), as well as the stemness potential of stem cells (Garcia-Prat *et al.* 2016; Garcia-Prat *et al.* 2017), represent already established age-associated pathways. To determine whether they were mechanistically involved -at least in part- in the AT-1 sTg phenotype, we analyzed whole tissue activation of Igf-1r signaling (**Figure S4a,b**); we also treated cultured MEF with Igf-1 (**Figure S4c,d**). However, we did not observe increased Igf-1r signaling in AT-1 sTg mice when compared to WT littermates (**Figure S4**). Similarly, no differences were detected in the percentages of bone marrow $Lin^{-}Sca^{+}c\text{-}Kit^{+}$ ($L^{-}S^{+}K^{+}$), multipotent progenitor (MPP; $L^{-}S^{+}K^{+}$,$CD48^{+}$, $CD150^{-}$), long-term hematopoietic stem cell (HSC) (LT-HSC; $L^{-}S^{+}K^{+}$,$CD48^{-}$, $CD150^{+}$), or short-term HSC (ST-HSC; $L^{-}S^{+}K^{+}$,$CD48^{-}$, $CD150^{-}$) populations from bone marrow of WT and AT-1 sTg mice, suggesting no intrinsic block in stemness potential (**Figure S5a**). Next, we transplanted WT and AT-1 sTg bone marrow (CD45.2) into lethally irradiated recipient mice with CD45.1 spleen cells as a supporting cell population and CD45.1 bone marrow cells. Again, no significant differences in contribution of CD45.2 donor cells to bone marrow was observed in WT vs. AT-1 sTg transplantation (**Figure S5b,c**).

Many human progeroid syndromes are characterized by nuclear instability where the primary defect is in the architecture and shape of the nuclear envelope; associated animal models reproduce the nuclear instability and mimic the progeroid phenotype (reviewed in (Kubben & Misteli 2017)). However, direct assessment of AT-1 sTg mice did not reveal any morphological aberration of the nucleus (**Figure S6**).

When taken together, the above results suggest that the reduced Atg9a-Fam134b-LC3β and Atg9a-Sec62-LC3β interaction, and the consequent block in reticulophagy with changes in efficiency of the secretory pathway are solely responsible for the progeria-like phenotype of AT-1 sTg mice.

**2.5 Inhibition of the ATases rescues the AT-1 sTg phenotype**

In addition to AT-1, which maintains the supply of acetyl-CoA to the ER lumen, the acetylation machinery includes two acetyltransferases, ATase1 and ATase2, which use acetyl-CoA to carry out the reaction of Nε-lysine acetylation (Ko & Puglielli 2009). The ATases are ER-resident membrane proteins and act down-stream of AT-1 (see **Figure 6a**). We previously reported the identification of ATase1/ATase2 specific inhibitors (Ding *et al.* 2012); we also reported the successful use of one of these compounds (6-chloro-5H-benzo[a]phenoxazin-5-one; referred to as compound 9) in a mouse model of Alzheimer's disease (Peng *et al.* 2016). Compound 9 is a powerful inhibitor of both ATases (Ding *et al.* 2012); it reduces the acetylation of Atg9a, improves the proteostatic functions of the ER, and is orally absorbed (Peng *et al.* 2016). Therefore, we treated AT-1 sTg mice with oral formulations of the compound (50 mg/kg/day (Peng *et al.* 2016)). We argued that if indeed the AT-1 sTg phenotype is caused by defective reticulophagy and defective elimination of toxic protein aggregates that form within the ER, then restoring the proteostatic functions of the ER by acting downstream of AT-1 is expected to ameliorate or rescue the phenotype. As an additional control to this study, we added a group of animals fed a Dox-containing diet to turn off the expression of AT-1 itself (see **Figure 1a**). In both cases, compound 9 and Dox were administered at weaning (postnatal day 22-25) when the initial disease phenotypes were already manifested.

Inhibition of the ATase1 and ATase2 by compound 9 rescued the progeria-like phenotype of AT-1 sTg mice. Indeed, the animals looked healthy, did not develop skin lesions, alopecia, rectal prolapse, or lordokyphosis (**Figure 6b,c**) and were able to gain weight as a function of age (**Figure 6d**). Importantly, compound 9 also rescued the lifespan of the animals (**Figure 6e**). Post-mortem analysis of 8-month old animals confirmed our general assessment. Compound 9-treated mice had normal fat pads and did not display muscle atrophy (**Figure 6f**). A complete blood count showed no evidence of anemia, which was paralleled by a normal sized spleen and no evidence of extramedullary erythropoiesis (**Figure S7a,b**). The lymph nodes were overall normal (**Figure S6c**); this result was paralleled by normalization of circulating inflammatory molecules (**Figure S7d**), and absence of SA-β-Gal activation (**Figure S7e,f**). Compound 9-treated mice also displayed normal bone mineral density (**Figure S7g**). Finally, compound 9 was able to rescue the metabolic aspects of the AT-1 sTg phenotype, including food intake (**Figure S7h**), circulating levels of glucose (**Figure S7i**), and cholesterolemia (**Figure S7j**).

Next, we determined Atg9a-Fam134b interaction as well as levels of Fam134b on ER structures following compound 9 treatment. Again, we observed that AT-1 sTg mice displayed reduced Atg9a-Fam134 interaction and increased ER membrane-associated Fam134b levels; however, both findings were completely normalized by compound 9 treatment (**Figure 7a-d**). Indeed, compound 9 restored Atg9a-Fam134b interaction (**Figure 7a,b**) and normalized Fam134b levels (**Figure 7c,d**). A similar result was observed with Sec62. In fact, compound 9 restored the Atg9a-Sec62 interaction at the ER membrane

(**Figure 7e,f**). Finally, compound 9 rescued the membrane expansion and reorganization of the ER observed in AT-1 sTg mice (**Figure 7g,h**).

In conclusion, the above results show that restoring the proteostatic functions of the ER by inhibiting ATase1 and ATase2 down-stream of AT-1 rescues the progeria-like phenotype of AT-1 sTg mice; they also support the notion that a block in Atg9a-Fam134b-LC3b and Atg9a-Sec62-LC3β interaction and the consequent defect in reticulophagy is at the basis of the AT-1 sTg phenotype (**Figure S8**). Although with some minor differences, the rescue elicited by compound 9 treatment was overall comparable to that of Dox, which in this study acted as our genetic control (see **Figures 6-7 and S7**). It is also important to stress that for our post-mortem analysis we used 8-month old animals, which corresponds to approximately twice the lifespan of untreated AT-1 sTg mice, thus indicating that the protective effects of compound 9 were long lasting.



## 3. DISCUSSION

### 3.1 Increased acetyl-CoA flux into the ER causes a progeria-like phenotype

Acetyl-CoA is a central metabolite that is key to many biochemical and cellular pathways. Acetyl-CoA also acts as the donor of the acetyl group in all reactions of Nε-lysine acetylation. Here, we report that increased acetyl-CoA flux from the cytosol to the ER lumen, as caused by systemic overexpression of human AT-1 in the mouse, causes a progeria-like phenotype with metabolic alterations. Segmental progerias typically manifest with severe debilitating symptoms and reduced lifespan. At birth, patients are typically smaller and display facial dysmorphism; as they grow, they develop a complex phenotype that often mimics accelerated forms of pathogenic aging. Segmental progerias include Hutchinson-Gilford, Cokayne, Werner, Bloom, and Rothmund-Thompsons syndromes, among others (Swahari & Nakamura 2016; Gonzalo *et al.* 2017; Karikkineth *et al.* 2017; Kubben & Misteli 2017).

Almost all human progeroid syndromes are characterized by nuclear and/or genomic instability where the primary defect is in the architecture of the nuclear envelope or in the DNA repairing machinery; associated animal models reproduce the nuclear and genomic instability and mimic the progeroid phenotype (reviewed in (Kubben & Misteli 2017)). Exceptions to the above are the p53/p44 and the AT-1 sTg systems. In the case of p53/p44, the primary defect is in the N-terminal regulatory functions of the p53 protein, which leads to reduced stemness potential of stem cells as well as hyperactivation of IGF-1R signaling (Tyner *et al.* 2002; Campisi 2004; Maier *et al.* 2004; Pehar *et al.* 2014; Lessel *et al.* 2017). AT-1 sTg mice display many features that are in line with classical segmental progerias, such as reduced growth, alopecia, skin lesions, rectal prolapse, osteoporosis, cardiomegaly, muscle atrophy, reduced fertility, and systemic inflammation. Unlike classical progerias, they do not display nuclear/genomic instability, reduced stemness potential of stem cells, or hyperactivation of IGF-1R signaling. Also in contrast with classical progerias, AT-1 sTg mice display metabolic-linked features that are not typically observed in progeria patients. We contend that the AT-1 sTg mouse represents the first model of progeria-like phenotype where the primary defect is in the regulation of intracellular acetyl-CoA flux, reticulophagy and proteostatic functions of the ER. In light of the known association between dysfunctional autophagy and age-associated diseases (Madeo *et al.* 2010; Kroemer 2015; Madeo *et al.* 2015), we can speculate that AT-1 sTg mice will offer new mechanistic and therapeutic avenues for several age-associated diseases.

**3.2 The progeria-like phenotype of AT-1 sTg mice is caused by a block in reticulophagy**

Our data suggest that defects in reticulophagy, perhaps accompanied by opposite changes in efficiency of the secretory pathway (Hullinger *et al.* 2016; Peng & Puglielli 2016), may causally contribute to the progeria-like phenotype of the AT-1 sTg mice. In AT-1 sTg mice, reticulophagy is linked to the acetylation status of Atg9 indicating that acetyl-coA flux is a key input for maintenance of ER homeostatic mechanisms (see **Figure S8**). We have previously shown that Atg9a acts as a sensor of the ER acetylation machinery; indeed, downregulation or expression of hypomorphic AT-1 lowers levels of acetylation of Atg9a and induces autophagy, while overexpression of AT-1 leads to increased acetylation of Atg9a and a block in autophagy induction (Pehar *et al.* 2012; Peng *et al.* 2014; Peng & Puglielli 2016). Importantly, gain-of-acetylation and loss-of-acetylation mutants of Atg9a can recapitulate the events reported above, thus providing mechanistic support (Pehar *et al.* 2012).

New results reported in this study indicate that functional Atg9a-Fam134b and Atg9a-Sec62 association is an initial and essential step for reticulophagy and that these interactions can occur only when Atg9a is not acetylated, highlighting the importance of acetylation on multiple levels in proteostatic control (see **Figure S8**). Fam134b is an integral ER membrane protein that acts as a “receptor” for

reticulophagy (Khaminets *et al.* 2015; Mochida *et al.* 2015; Rubinsztein 2015). It was recently identified in both yeast and mammalian cells (Khaminets *et al.* 2015; Mochida *et al.* 2015; Rubinsztein 2015). Interestingly, Fam134b seems to preferentially localize on ER sheet-like (rough ER) structures, where the bulk of protein biosynthesis normally occurs, and might act as part of quality control to couple protein biosynthesis to disposal of unfolded/misfolded polypeptides (Nakatogawa & Mochida 2015). Sec62, an integral member of the ER translocon machinery, also seems to act as an ER-resident autophagy "receptor" (Fumagalli *et al.* 2016). Sec62 is also thought to be involved in coupling the insertion of newly-synthesized proteins into the ER with the regulatory mechanisms that detect and dispose of unfolded/misfolded polypeptides (Schuck 2016). Both Fam134b and Sec62 require physical interaction with LC3β to exert their functions (Khaminets *et al.* 2015; Mochida *et al.* 2015; Rubinsztein 2015; Fumagalli *et al.* 2016; Schuck 2016). The fact that Atg9a acetylation status directs the formation of Sec62 and Fam134b complexes, sequestering them from the essential binding partner LC3β, suggests coordination of events to influence reticulophagy (see **Figure S8**). The specific contribution of enhanced efficiency of the secretory pathway to the progeria phenotype of AT-1 sTg mice remains to be determined.

### 3.3 Biochemical inhibition of the ATases down-stream of AT-1 restores reticulophagy and rescues the progeria-like phenotype

The impact of pharmacological inhibition of the acetyltransferases, ATase1 and ATase2, is an exciting development and one that may have clinical application. ATase1 and ATase2 act down-stream of AT-1 to acetylate ER cargo proteins (Ko & Puglielli 2009), regulate the acetylation status of Atg9a, and are essential for the proteostatic functions of the ER acetylation machinery (Ding *et al.* 2014; Peng *et al.* 2016). Our study showed that inhibition of the ATases was able to restore the Atg9a-Fam134b-LC3β and Atg9a-Sec62-LC3β interaction at the ER membrane, and rescue the progeria-like phenotype of AT-1 sTg mice. Overexpression of AT-1 in the mouse seems to recapitulate the outcomes of children with duplications of the 3q25.31 locus (containing *AT-1/SLC33A1*). In this study, treatment with compound 9 was initiated at weaning when the disease manifestations were already developing. This suggests that strategies based on similar targeting might be effective in treating the human disease, where early diagnosis and early treatment could mitigate or even prevent disease manifestations.

While recognizing the intrinsic limitations of a single gene-directed progeria model, several aspects of the phenotype developed by AT-1 sTg mice mimic accelerated forms of pathogenic aging. Therefore, the model may provide insights into a range of age-related diseases and conditions, and studies on ATase1/ATase2 inhibitors might be relevant for chronic diseases linked to proteostatic dysfunction. For example, the entire ER acetylation machinery, AT-1 (Gomez Ravetti *et al.* 2010; Jonas *et al.* 2010) and

the ATases (Ding *et al.* 2012), is upregulated in patients with late-onset Alzheimer's disease, the most common form of age-associated dementia. Importantly, both haploinsufficiency of AT-1 and biochemical inhibition of the ATases using compound 9 were able to rescue the Alzheimer's disease-like phenotype in the mouse (Duran-Aniotz *et al.* 2016; Peng *et al.* 2016). We are eager to further explore these models and strategies that we believe will have utility in a broader context of aging and age-related disease.

### 3.4 Conclusion

In conclusion, our study shows that systemic overexpression of AT-1 in the mouse causes a progeria-like phenotype with metabolic alterations. Mechanistically, the phenotype is caused by a block in Atg9a-Fam134b-LC3β and Atg9a-Sec62-LC3β interaction, which prevents the induction of reticulophagy. Our study also shows that restoring the proteostatic functions of the ER, by targeting the ATases down-stream of AT-1, can rescue the mouse phenotype, thus suggesting that ATase1/ATase2 inhibitors might offer translational opportunities for patients with *AT-1*/*SLC33A1* duplications and for the mitigation of different age-associated diseases. Finally, this study sets the foundation for new inquiries into the mechanisms that regulate intracellular acetyl-CoA flux and availability, and how they can influence disease phenotypes that have not been traditionally viewed as primarily driven by metabolic changes.

## 4. EXPERIMENTAL PROCEDURES

### 4. 1. Transgenic animals

pTRE-AT-1 Tg mice were described previously (Hullinger *et al.* 2016). ROSA:LNL:tTA (Gt(ROSA)26Sor$^{tm1(tTA)Roos}$/J; JAX Stock No: 011008) were bred to EIIa-Cre (B6.FVB-Tg(EIIa cre)C5379Lmgd/J; JAX Stock No: 003724), generating Rosa26:tTA mice which universally express tTA. Rosa26:tTA mice were then crossed with pTRE-AT-1 mice to generate ROSA26:tTA;pTRE-AT-1 (referred to as AT-1 sTg) mice. Genotyping from tail DNA was performed

using the following primers: AT-1 forward (5′-AAT CTG GGA AAC TGG CCT TCT-3′), AT-1 reverse (5′-TAT TAC CGC CTT TGA GTG AGC TGA-3′), Rosa forward (5′-AAA GTC GCT CTG AGT TGT TAT-3′), Rosa reverse (5′-GCG AAG AGT TTG TCC TCA ACC-3′). Both males and females were studied. Wild-type (WT) littermates were used as controls throughout our study. Unless specified, living AT-1 sTg mice were studied at the age of approx. 3 months.

The rodent diet with Compound 9 was manufactured by Bio-Serv. The food with Doxycycline (200 mg/kg) was purchased from Bio-Serv. The same diet without Compound 9 or Doxycycline served as the control diet.

All animal experiments were carried out in accordance with the NIH Guide for the Care and Use of Laboratory Animals and were approved by the Institutional Animal Care and Use Committee of the University of Wisconsin-Madison and the Madison Veterans Administration Hospital.

**4.2. Cell cultures**

Mouse embryonic fibroblasts (MEFs) from wild-type and AT-1 sTg mice were prepared as described previously (Peng *et al.* 2014). Further details are in supporting information.

**4.3. Hepatocyte isolation**

Hepatocytes were isolated and analyzed as described in supporting information.

**4.4. Protein extraction, Western blotting, and immunoprecipitation**

Protein extraction, Western blotting, and immunoprecipitation techniques are described in supporting information.

**4.5. Dot blots**

Dot blot analysis was performed as described in supporting information.

**4.6. Real-time PCR**

Real-time PCR was performed as described before (Jonas *et al.* 2010). Further details and in supporting information.

**4.7. Histology and bone histomorphometry**

Histology and bone histomorphometry were performed as described in supporting information.

**4.8. Faxitron radiography and dual-energy X-ray absorptiometry (DEXA)**

DEXA analysis was conducted as described in supporting information.

**4.9. Whole blood, serum and plasma analytes**

Blood, serum and plasma analytes were determined as in supporting information.

**4.10. Blood and bone marrow smear examination**

Fresh whole blood or bone marrow samples were smeared as in supporting information.

**4.11. Flow Cytometry**

Flow cytometry was performed as in supporting information.

**4.12. Erythroid progenitor assays**

Erithroid progenitor assays was performed as in supporting information.

**4.13. Bone marrow transplantation**

Bone marrow transplantation experiments were performed as described previously (Wang *et al.* 2011). Further details are in supporting information.

**4.14. Senescence associated β-galactosidase staining**

Senescence β Galactosidase staining was performed as in supporting information.

**4.15. OGTT, Glucose, Insulin and Glucagon assays**

OGTT, glucose, insulin and glucagon assays were performed as in supporting information.

**4.16. Echocardiography**

Transthoracic echocardiography was performed as described previously (Harris *et al.* 2002). Further details are in supporting information.

**4.17. Trafficking of newly synthetized glycoproteins**

Quantification of trafficking glycoproteins along the secretory pathway was performed as previously described (Hullinger *et al.* 2016). Further details are in supporting information.

**4.18. Statistics**

Data analysis was performed using GraphPad InStat 3.06 statistical software (GraphPad Software Inc.). Data are expressed as mean ± standard deviation (SD). Comparison of the means was performed using Student's t-test or one-way ANOVA followed by Tukey-Kramer multiple comparisons test. For lifespan assessment, data were analyzed with the Kaplan-Meier lifespan test and log-rank test using GraphPad Prism version 7.03 (GraphPad Software). Differences were declared statistically significant if $p<0.05$.



**ACKNOWLEDGEMENTS**

We thank Dr. Albee Messing for critical reading of an early version of this manuscript. We thank Dr. Maria M. Mihaylova and Nicole Cummings for advice on hepatocyte isolation and culture; Dr. Peter Muir, Vicki Kalscheur, and Zhengling Hao at the UW Bone Core Facility for their help with bone analysis; Dr. Brigitte Raabe and Yang Pong for their help with the mouse colony.

This work was supported by the NIH (NS094154 and AG053937 to LP; AG057408 to LP and RMA; DK50107 to EHB.; HL113066 and CA152108 to JZ; DK102948 and DK108259 to ADA; AG041765 and AG051974 to DWL); a core grant to the Waisman Center from NICHD-U54 HD090256; the Glenn Foundation to DWL; and the American Federation for Aging Research to DWL. IAD was supported by T32 AG000213. SIAA was supported in part by the American Diabetes Association. This work was also supported using resources and facilities of the William S. Middleton Memorial Veterans Hospital

(Madison, WI). SIM imaging was performed at the Biochemistry Optical Core of the University of Wisconsin-Madison (Madison, WI).



## AUTHOR CONTRIBUTION

YP, SLS, VCB, IAD, KJH, GK, KLS, RS, and SIAA performed experiments and all authors analyzed data. EHB, JZ, MPK, ADA, TAH, EK-G, DWL, RMA and LP provided critical advice for the experiments. LP designed the overall study and wrote the manuscript with input from all authors.

## CONFLICT OF INTEREST

DWL has received funding from, and is a scientific advisory board member of, Delos Pharmaceuticals, which seeks to develop novel, selective mTOR inhibitors for the treatment of various diseases. DWL's spouse is an employee of DaVita Clinical Research.

All others Authors have no conflict of interests to disclose.

## REFERENCES

Campisi, J. (2004). Fragile fugue: p53 in aging, cancer and IGF signaling. *Nat Med*. **10**, 231-232.

Chiplunkar, S., Bindu, P.S., Nagappa, M., Bineesh, C., Govindaraj, P., Gayathri, N., …Taly, A.B. (2016). Huppke-Brendel syndrome in a seven months old boy with a novel 2-bp deletion in SLC33A1. *Metab Brain Dis*. **31**, 1195-1198.

Dempski, R.E., Jr., Imperiali, B. (2002). Oligosaccharyl transferase: gatekeeper to the secretory pathway. *Curr Opin Chem Biol*. **6**, 844-850.

Ding, Y., Dellisanti, C.D., Ko, M.H., Czajkowski, C., Puglielli, L. (2014). The endoplasmic reticulum-based acetyltransferases, ATase1 and ATase2, associate with the oligosaccharyl-transferase to acetylate correctly folded polypeptides. *J Biol Chem.* **289**, 32044-32055.

Ding, Y., Ko, M.H., Pehar,M., Kotch, F., Peters, N.R., Luo, Y., … Puglielli, L. (2012). Biochemical inhibition of the acetyltansferases ATase1 and ATase2 reduces b-secretase (BACE1) levels and Ab generation. *J Biol Chem*. **287**, 8424-8433.

Duran-Aniotz, C., Cornejo, V.H., Hetz, C. (2016). Targeting endoplasmic reticulum acetylation to restore proteostasis in Alzheimer's disease. *Brain*. **139**, 650-652.

Fumagalli, F., Noack, J., Bergmann, T.J., Cebollero, E., Pisoni, G.B., Fasana, E., … Molinari, M. (2016). Translocon component Sec62 acts in endoplasmic reticulum turnover during stress recovery. *Nat Cell Biol*. **18**, 1173-1184.

Garcia-Prat, L., Martinez-Vicente, M., Perdiguero, E., Ortet, L., Rodriguez-Ubreva, J., Rebollo, E., … Munoz-Canoves, P. (2016). Autophagy maintains stemness by preventing senescence. *Nature*. **529**, 37-42.

Garcia-Prat, L., Sousa-Victor, P., Munoz-Canoves, P. (2017). Proteostatic and Metabolic Control of Stemness. *Cell Stem Cell*. **20**, 593-608.

Gomez Ravetti, M., Rosso, O.A., Berretta, R., Moscato, P. (2010). Uncovering molecular biomarkers that correlate cognitive decline with the changes of hippocampus' gene expression profiles in Alzheimer's disease. *PLoS One*. **5**, e10153.

Gonzalo, S., Kreienkamp, R., Askjaer, P. (2017). Hutchinson-Gilford Progeria Syndrome: A premature aging disease caused by LMNA gene mutations. *Ageing Res Rev*. **33**, 18-29.

Harris, S.P. Bartley, C.R., Hacker, T.A., McDonald, K.S., Douglas, P.S., Greaser, M.L., … Moss, R.L. (2002). Hypertrophic cardiomyopathy in cardiac myosin binding protein-C knockout mice. *Circ Res*. **90**, 594-601.

Hullinger, R., Li, M., Wang, J., Peng, Y., Dowell, J.A., Bomba-Warczak, E., … Puglielli, L. (2016). Increased expression of AT-1/SLC33A1 causes an autistic-like phenotype in mice by affecting dendritic branching and spine formation. *J Exp Med*. **213**, 1267-1284.

Huppke, P., Brendel, C., Kalscheuer, V., Korenke, G.C., Marquardt, I., Freisinger, P., … Gartner, J. (2012). Mutations in SLC33A1 cause a lethal autosomal-recessive disorder with congenital cataracts, hearing loss, and low serum copper and ceruloplasmin. *Am J Hum Genet*. **90**, 61-68.

Jeon, O.H., Kim, C., Laberge, R.M., Demaria, M., Rathod, S., Vasserot, A.P., … Elisseeff, J.H. (2017). Local clearance of senescent cells attenuates the development of post-traumatic osteoarthritis and creates a pro-regenerative environment. *Nat Med*. **23**, 775-781.

Jonas, M.C., Pehar, M., Puglielli, L. (2010). AT-1 is the ER membrane acetyl-CoA transporter and is essential for cell viability. *J Cell Sci*. **123**, 3378-3388.

Kang, C., Xu, Q., Martin, T.D., Li, M.Z., Demaria, M., Aron, L., … Elledge, S.J. (2015). The DNA damage response induces inflammation and senescence by inhibiting autophagy of GATA4. *Science*. **349**, aaa5612.

Karikkineth, A.C., Scheibye-Knudsen, M., Fivenson, E., Croteau, D.L., Bohr, V.A. (2017). Cockayne syndrome: Clinical features, model systems and pathways. *Ageing Res Rev*. **33**, 3-17.

Kenyon, C. (2005). The plasticity of aging: insights from long-lived mutants. *Cell*. **120**, 449-460.

Khaminets, A., Heinrich, T., Mari, M., Grumati, P., Huebner, A.K., Akutsu, M., … Dikic I. (2015). Regulation of endoplasmic reticulum turnover by selective autophagy. *Nature*. **522**, 354-358.

Kleizen, B., Braakman, I. (2004). Protein folding and quality control in the endoplasmic reticulum. *Curr Opin Cell Biol*. **16**, 343-349.

Klionsky, D.J., Abdelmohsen, K., Abe, A., Abedin, M.J., Abeliovich, H., Acevedo Arozena, A., … Zughaier, S.M. (2016). Guidelines for the use and interpretation of assays for monitoring autophagy (3rd edition). *Autophagy*. **12**, 1-222.

Ko, M.H., Puglielli, L. (2009). Two Endoplasmic Reticulum (ER)/ER Golgi Intermediate Compartment-based Lysine Acetyltransferases Post-translationally Regulate BACE1 Levels. *J Biol Chem*. **284**, 2482-2492.

Kroemer, G. (2015). Autophagy: a druggable process that is deregulated in aging and human disease. *J Clin Invest*. **125**, 1-4.

Kubben, N., Misteli, T. (2017). Shared molecular and cellular mechanisms of premature ageing and ageing-associated diseases. *Nat Rev Mol Cell Biol*. **18**, 595-609.

Kuro-o, M., Matsumura, Y., Aizawa, H., Kawaguchi, H., Suga, T., Utsugi, T., … Nabeshima, Y.I. (1997). Mutation of the mouse klotho gene leads to a syndrome resembling ageing. *Nature*. **390**, 45-51.

Lennemann, N.J., Coyne, C.B. (2017). Dengue and Zika viruses subvert reticulophagy by NS2B3-mediated cleavage of FAM134B. *Autophagy*. **13**, 322-332.

Lessel, D., Wu, D., Trujillo, C., Ramezani, T., Lessel, I., Alwasiyah, M.K., … Kubisch, C. (2017). Dysfunction of the MDM2/p53 axis is linked to premature aging. *J Clin Invest*. **127**, 3598-3608.

Liao, C.Y., Kennedy, B.K. (2014). Mouse models and aging: longevity and progeria. *Curr Top Dev Biol*. **109**, 249-285.

Lin, P., Li, J., Liu, Q., Mao, F., Qiu, R., Hu, H., … Gong, Y. (2008). A missense mutation in SLC33A1, which encodes the acetyl-CoA transporter, causes autosomal-dominant spastic paraplegia (SPG42). *Am J Hum Genet*. **83**, 752-759.

Longo, V.D., Finch, C.E. (2003). Evolutionary medicine: from dwarf model systems to healthy centenarians? *Science*. **299**, 1342-1346.

Madeo, F., Tavernarakis, N., Kroemer, G. (2010). Can autophagy promote longevity? *Nat Cell Biol*. **12**, 842-846.

Madeo, F., Zimmermann, A., Maiuri, M.C., Kroemer, G. (2015). Essential role for autophagy in life span extension. *J Clin Invest*. **125**, 85-93.

Maier, B., Gluba, W., Bernier, B., Turner, T., Mohammad, K., Guise, T., … Scrable, H. (2004). Modulation of mammalian life span by the short isoform of p53. *Genes Dev*. **18**, 306-319.

Milman, S., Huffman, D.M., Barzilai, N. (2016). The Somatotropic Axis in Human Aging: Framework for the Current State of Knowledge and Future Research. *Cell Metab*. **23**, 980-989.

Mochida, K., Oikawa, Y., Kimura, Y., Kirisako, H., Hirano, H., Ohsumi, Y., Nakatogawa, H. (2015). Receptor-mediated selective autophagy degrades the endoplasmic reticulum and the nucleus. *Nature*. **522**, 359-362.

Nakatogawa, H., Mochida, K. (2015). Reticulophagy and nucleophagy: New findings and unsolved issues. *Autophagy*. **11**, 2377-2378.

Ovadya, Y., Krizhanovsky, V. (2014). Senescent cells: SASPected drivers of age-related pathologies. *Biogerontology*. **15**, 627-642.

Pehar, M., Jonas, M.C., Hare, T.M., Puglielli, L. (2012). SLC33A1/AT-1 protein regulates the induction of autophagy downstream of IRE1/XBP1 pathway. *J Biol Chem*. **287**, 29921-29930.

Pehar, M., Ko, M.H., Li, M., Scrable, H., Puglielli, L. (2014). P44, the 'longevity-assurance' isoform of P53, regulates tau phosphorylation and is activated in an age-dependent fashion. *Aging Cell*. **13**, 449-456.

Pehar, M., O'Riordan, K.J., Burns-Cusato, M., Andrzejewski, M.E., del Alcazar, C.G., Burger, C., … Puglielli, L. (2010). Altered longevity-assurance activity of p53:p44 in the mouse causes memory loss, neurodegeneration and premature death. *Aging Cell*. **9**, 174-190.

Peng, Y., Kim, M.J., Hullinger, R., O'Riordan, K.J., Burger, C., Pehar, M., Puglielli, L. (2016). Improved proteostasis in the secretory pathway rescues Alzheimer's disease in the mouse. *Brain*. **139**, 937-952.

Peng, Y., Li, M., Clarkson, B.D., Pehar, M., Lao, P.J., Hillmer, A.T., … Puglielli, L. (2014). Deficient Import of Acetyl-CoA into the ER Lumen Causes Neurodegeneration and Propensity to Infections, Inflammation, and Cancer. *J Neurosci*. **34**, 6772-6789.

Peng, Y., Puglielli, L. (2016). N-lysine acetylation in the lumen of the endoplasmic reticulum: A way to regulate autophagy and maintain protein homeostasis in the secretory pathway. *Autophagy*. **12**, 1051-1052.

Pivnick, E.K., Angle, B., Kaufman, R.A., Hall, B.D., Pitukcheewanont, P., Hersh, J.H., … Ward, J.C. (2000). Neonatal progeroid (Wiedemann-Rautenstrauch) syndrome: report of five new cases and review. *Am J Med Genet*. **90**, 131-140.

Polymeropoulos, M.H., Lavedan, C., Leroy, E., Ide, S.E., Dehejia, A., Dutra, A., … Nussbaum, R.L. (1997). Mutation in the alpha-synuclein gene identified in families with Parkinson's disease. *Science*. **276**, 2045-2047.

Rubinsztein, D.C. (2015). Cell biology: Receptors for selective recycling. *Nature*. **522**, 291-292.

Schuck, S. (2016). On keeping the right ER size. *Nat Cell Biol*. **18**, 1118-1119.

Swahari, V., Nakamura, A. (2016). Speeding up the clock: The past, present and future of progeria. *Dev Growth Differ*. **58**, 116-130.

Tchkonia, T., Zhu, Y., van Deursen, J., Campisi, J., Kirkland, J.L. (2013). Cellular senescence and the senescent secretory phenotype: therapeutic opportunities. *J Clin Invest*. **123**, 966-972.

Trombetta, E.S., Parodi, A.J. (2003). Quality control and protein folding in the secretory pathway. *Annu Rev Cell Dev Biol*. **19**, 649-676.

Tyner, S.D., Venkatachalam, S., Choi, J., Jones, S., Ghebranious, N., Igelmann, H., … Donehower, L.A. (2002). p53 mutant mice that display early ageing-associated phenotypes. *Nature*. **415**, 45-53.

Wang, J., Liu, Y., Li, Z., Wang, Z., Tan, L.X., Ryu, M.J., … Zhang, J. (2011). Endogenous oncogenic Nras mutation initiates hematopoietic malignancies in a dose- and cell type-dependent manner. *Blood*. **118**, 368-379.



**SUPPORTING INFORMATION**

- Experimental Procedures
- Figures S1-S8

**Table 1. Observed phenotype of AT-1 sTg mice**

| | |
|---|---|
| Median lifespan | Greatly reduced (males, 96 days; females, 81 days) |
| Maximum lifespan | Greatly reduced (males, 142 days; females, 147 days) |
| Body weight | Reduced |
| Dysmorphism | Observed |
| Major organ mass | Increased (exception: uterus, decreased) |
| Fertility | Males, normal; females, reduced |
| Adipose tissue | Reduced |
| Lordokyphosis | Modest or absent |
| Cardiomegaly | Pronounced |
| Osteoporosis | Pronounced |
| Hair loss | Pronounced |

| | |
|---|---|
| Hair regrowth | Greatly reduced |
| Skin lesions | Pronounced |
| Wound repair | Retarded |
| Muscle atrophy | Modest to severe |
| Cataracts | Normal (as in WT) |
| Dermal thickness | Reduced |
| Rectal prolapse | Common |
| Systemic inflammation | Pronounced |
| Peripheral WBC | Altered (B cell and neutrophil expansion) |
| Peripheral RBC | Altered (anemia) |
| Serum glucose/insulin | Reduced |
| Serum lipids | Hypocholesterolemia |
| Glucose tolerance | Altered |



**FIGURE LEGENDS**

**Figure 1. AT-1 sTg mice are smaller and have a short lifespan.** (a) AT-1 sTg mice were generated with an inducible Tet-Off expression system under the control of the Rosa26 locus for systemic overexpression. (b) Western blots showing AT-1 overexpression in different tissues (*1*, WT; *2*, AT-1 sTg). (c) Representative AT-1 sTg mouse and WT littermate when 28 and 55 days old. (d) Body weight of male and female WT and AT-1 sTg mice across their lifespan. (e) Lifespan of AT-1 sTg mice

(*maximum lifespan*, males=142 days, females=147 days, $p<0.0005$; *median lifespan*, males=96 days, females=81 days, $p<0.0005$). Bars represent mean ± SD. $^{*}p<0.05$; $^{**}p<0.005$; $^{\#}p<0.0005$.



**Figure 2. AT-1 sTg mice display progeria-like features.** (a) Examination of WT and AT-1 sTg mice. Reduced fat accumulation and splenomegaly are evident in both AT-1 sTg males and females. (b) Total body fat in WT and AT-1 sTg mice as determined by dual-energy X-ray (DEXA) scanning (males, n=7; females, n=8). (c) Food intake of WT and AT-1 sTg mice (males, n=5; females, n=5). (d) Skeletal muscle histology. (e) Weight of major organs. *Inset* shows uterus. (f) Skin alterations and rectal prolapse in AT-1 sTg mice. (g) H&E staining of a skin section from AT-1 sTg mice. (h, i) Faxitron X-ray (femur) (h) and bone mineral density (i) of WT and AT-1 sTg mice (WT, n=8; AT-1 sTg, n=8). (j) Goldner's trichrome stain of femur sections. (k, l) Echocardiographic assessment of WT and AT-1 sTg mice (WT, n=8; AT-1 sTg, n=8). *LVID;d*, left ventricular internal diameter end diastole; *LVPW;d*, left ventricular posterior wall end diastole; *LVAW;d*, left ventricular anterior wall end diastole. Bars represent mean ± SD. $^{*}p<0.05$, $^{**}p<0.005$, $^{\#}p<0.0005$.

**Figure 3. AT-1 sTg mice display defective hematopoiesis, and reduced levels of circulating glucose, insulin and cholesterol.** (a) Hematologic parameters of WT and AT-1 sTg mice (males, n=4; females, n=6). *WBC*, white blood cells; *RBC*, red blood cells; *HCT*, hematocrit; *Hb*, hemoglobin. (b) Representative images of whole spleen from WT and AT-1 sTg mice. (c, d) Quantitative blood (c) and bone marrow (d) smears in WT and AT-1 sTg mice (males, n=4; females, n=4). (e) Quantitation (*left*) and representative images (*right*) of Colony Forming Unit-Erythroid (CFU-E) colonies 2 days after plating splenic cells ($1 \times 10^5$) from WT (n=3) and AT-1 sTg (n=3) mice in methylcellulose containing Epo, SCF, IL-3, and IL-6. (f) Quantitation (*left*) and representative images (*right*) of Burst Forming Unit-Erythroid (BFU-E) colonies 5 days after plating splenic cells ($1 \times 10^5$) from WT (n=3) and AT-1 sTg (n=3) mice in methylcellulose containing Epo, SCF, IL-3, and IL-6. (g, h) Fasting levels of glucose (g) and insulin (h) in plasma (males, n=5; females, n=5). (i, j) Oral glucose tolerance test (OGTT) in WT and AT-1 sTg mice (males, n=5; females, n=5). $AUC_{glucose}$ (i) and $AUC_{insulin}$ (j) are shown. (k) Plasma lipid profile in WT and AT-1 sTg mice (males, n=5; females, n=5). Bars represent mean ± SD. $^{*}p<0.05$, $^{**}p<0.005$, $^{\#}p<0.0005$.

**Figure 4. AT-1 sTg mice display systemic and tissue inflammation.** (a) Weight of axillary lymph nodes in WT and AT-1 sTg mice (n=6 per group). (b) Plasma inflammatory markers (out of a total of 42 different analytes tested). *In red*, analytes that were changed in both males and females (males, n=6; females, n=6). (c, d) Dot-blot of tissue immunoglobulins determined with anti-mouse IgG. Representative images (c) and quantitation of results (d) are shown (*EC*, extracellular; *IC*, intracellular; *MB*, membrane-bound; *FA*, formic acid-soluble). The analysis was done in liver (WT, n=3; AT-1 sTg, n=3). (e, f) Western blot showing tissue immunoglobulins determined with anti-mouse IgG. Representative images (e) and quantitation of results (f) are shown (*EC*, extracellular; *IC*, intracellular; *Hc*, heavy chain; *Lc*, light chain). The analysis was done in liver (WT, n=3; AT-1 sTg, n=3). (g, h) Flow cytometry showing B cell (g), and neutrophil (h) population in bone marrow and peripheral blood (WT, n=3; AT-1 sTg, n=3). (i) Western blot showing p16 levels in liver. Representative images (left panel) and quantitation of results (right panel) are shown (WT, n=7; AT-1 sTg, n=7). (j) p21 mRNA quantitation in liver (WT, n=7; AT-1 sTg, n=7). (k, l) SA-β-Gal staining in liver and hepatocytes. Representative images (k) and quantitation of results (l) are shown (WT, n=3; AT-1 sTg, n=3). (m, n) Proliferation potential of cultured MEF expressed as proliferation rate at each passage (m; n=3 different MEF lines/group) and as cell number after plating (n; n=3 different MEF lines/group). Bars represent mean $\pm$ SD. $^{*}p<0.05$, $^{**}p<0.005$, $^{\#}p<0.0005$.

**Figure 5. AT-1 sTg mice display defective reticulophagy and expansion of the ER.** (a, b) Western blot showing levels of acetylated-Atg9a (Atg9a-Ac) in ER preparations from liver. Representative blots are shown in (a) while quantitation of results is shown in (b) (WT, n=3; AT-1 sTg, n=3). (c) Structure illumination microscopy (SIM) of ER in isolated hepatocytes showing size and morphology of sheet-like structures. (d, e) SIM showing Fam134b puncta on ER of isolated hepatocytes. *N*, nucleus. Quantitation of results is shown in (e) (WT, n=8; AT-1 sTg, n=7). (f) Fam134b mRNA quantitation in liver (WT, n=6; AT-1 sTg, n=5). (g, h) Western blot showing levels of Fam134b in ER preparations. Representative blots are shown in (g) while quantitation of results is shown in (h) (WT, n=4; AT-1 sTg, n=4). (i, j) SIM showing reduced Fam134b/LC3β co-localization on ER of isolated hepatocytes from AT-1 sTg mice. Quantitation of results is shown in (j) (WT, n=5; AT-1 sTg, n=5). (k, l) Western blot showing co-immunoprecipitation of Atg9a and Fam134b in WT and AT-1 sTg mice. Representative blots are shown

in (k) while quantitation of results is shown in (l) (WT, n=8; AT-1 sTg, n=8). (m, n) SIM showing reduced Sec62/LC3β co-localization on ER of isolated hepatocytes from AT-1 sTg mice. Quantitation of results is shown in (n) (WT, n=5; AT-1 sTg, n=5). (o, p) Western blot showing co-immunoprecipitation of Atg9a and Sec62 in WT and AT-1 sTg mice. Representative blots are shown in (o) while quantitation of results is shown in (p) (WT, n=7; AT-1 sTg, n=7). Bars represent mean ± SD. $^{*}p<0.05$, $^{**}p<0.005$, $^{\#}p<0.0005$.

**Figure 6. ATase1/ATase2 inhibition rescues the progeria-like phenotype and lifespan of AT-1 sTg mice.** (a) Schematic view of the ER acetylation machinery with compound 9 acting on the ATases downstream of AT-1. (b, c) Representative images of AT-1 sTg mice with and without compound 9 treatment. Dox treatment is shown for comparison. Mice at two different ages are shown. (d) Body weight of male and female AT-1 sTg mice with and without compound 9 treatment. Dox-treated AT-1 sTg mice are shown for comparison (n=16 for all groups). (e) Lifespan of AT-1 sTg mice with and without compound 9 treatment. Dox-treated AT-1 sTg mice are shown for comparison ($p<0.0005$, all *vs* AT-1 sTg with chow). (f) Postmortem examination of WT and AT-1 sTg mice treated with compound 9. Dox treatment is shown for comparison. Mice were 8 months old when examined. Bars represent mean ± SD. $^{**}p<0.005$; $^{\#}p<0.0005$.

**Figure 7. ATase1/ATase2 inhibition restores reticulophagy in AT-1 sTg mice**. (a, b) Western blot showing Atg9a-Fam134b interaction on the ER membrane of compound 9-treated AT-1 sTg mice. Dox-treated and 3 month-old AT-1 sTg mice are shown for comparison. Representative blots are shown in (a) while quantitation of results is shown in (b) (n=6 for all groups). (c, d) Western blot showing ER levels of Fam134b in compound 9-treated AT-1 sTg mice. Dox-treated and 3 month-old AT-1 sTg mice are shown for comparison. Representative blots are shown in (c) while quantitation of results is shown in (d) (n=6 for all groups). (e, f) Western blot showing Atg9a-Sec62 interaction on the ER membrane of compound 9-treated AT-1 sTg mice. Dox-treated and 3 month-old AT-1 sTg mice are shown for comparison. Representative blots are shown in (e) while quantitation of results is shown in (f) (n=6 for all groups). (g) Structure illumination microscopy (SIM) of ER in isolated hepatocytes from compound 9-treated AT-1 sTg mice. Dox-treated and 3 month-old AT-1 sTg mice are shown for comparison. *N*, nucleus. (h) High-

magnification images with Imaris-mediated reconstruction. Bars represent mean ± SD. $^{*}p<0.05$, $^{**}p<0.005$, $^{\#}p<0.0005$.

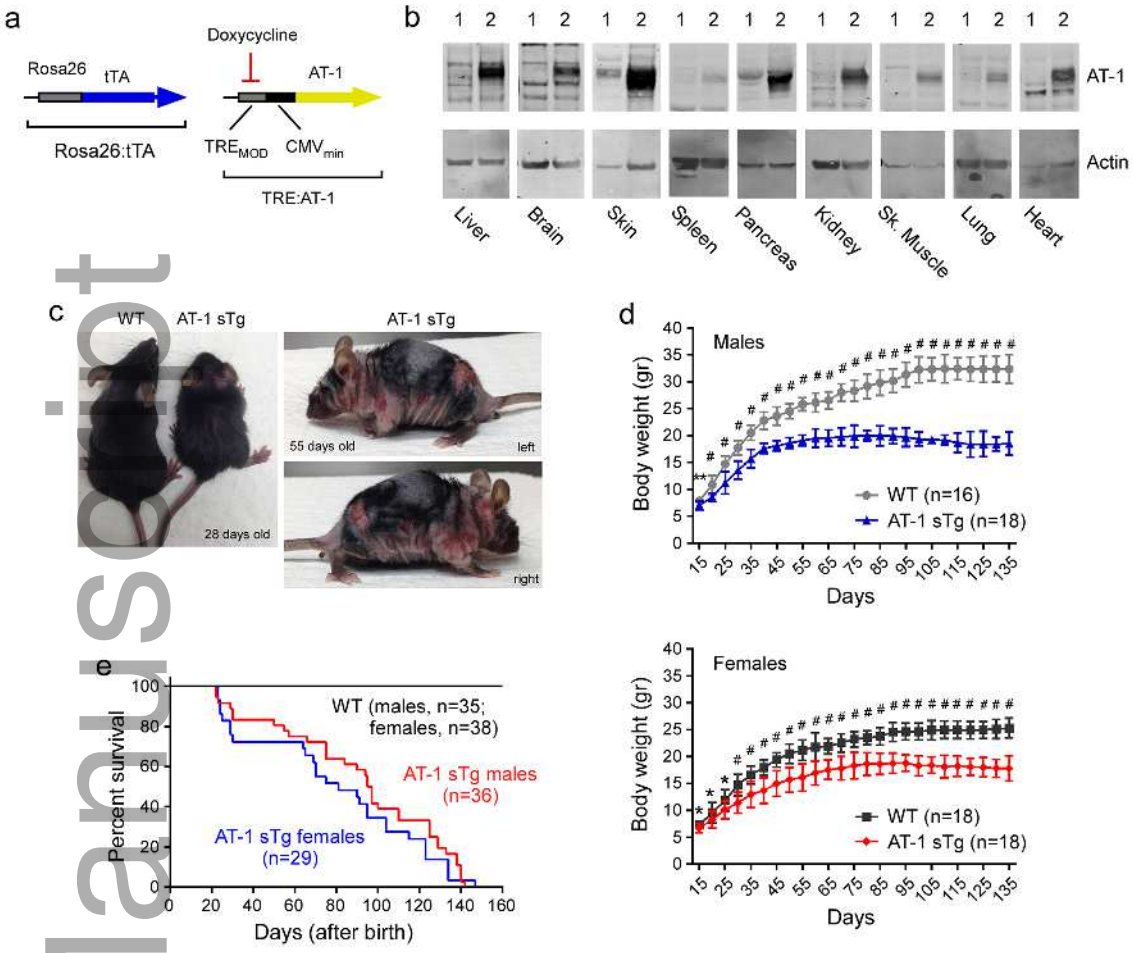


acel_12820_f1.tif

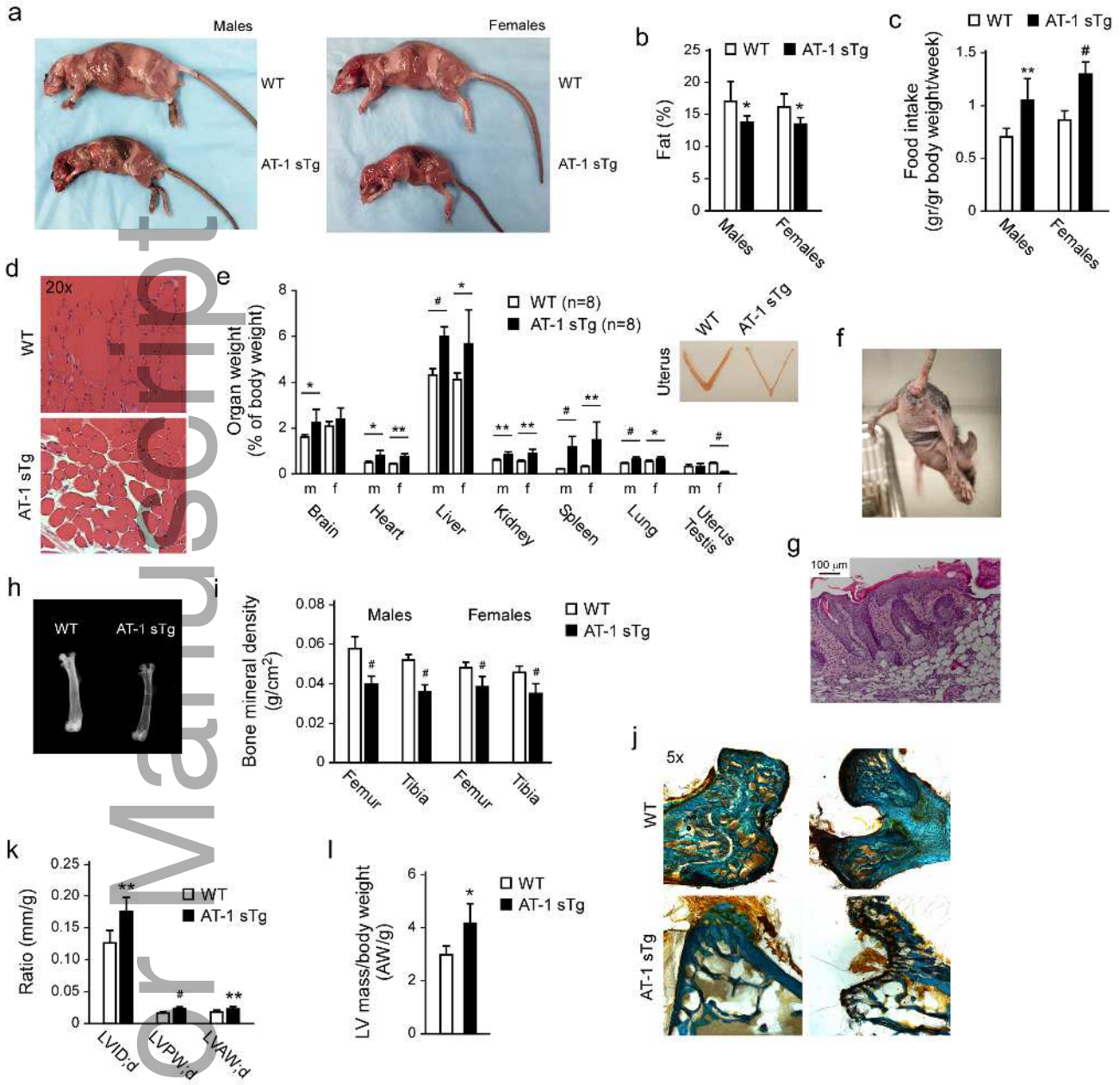


acel_12820_f2.tif

a

Complete blood count in WT and AT-1 sTg mice

| | | WT | AT-1 sTg | |
|---|---|---|---|---|
| Males | WBC (k/μl) | 3.9 ± 1.4 | 6.1 ± 6.6 | ns |
| | RBC (M/μl) | 10.5 ± 1.6 | 8.8 ± 2.2 | ns |
| | HCT (%) | 46.5 ± 8.8 | 42.7 ± 12.3 | ns |
| | Hb (g/dl) | 13.1 ± 2.3 | 11.2 ± 2.9 | ns |
| Females | WBC (k/μl) | 2.4 ± 1.3 | 4.7 ± 1.9 | ns |
| | RBC (M/μl) | 11.1 ± 2.2 | 7.1 ± 0.9 | p<0.05 |
| | HCT (%) | 52.5 ± 11.8 | 32.9 ± 3.5 | p<0.05 |
| | Hb (g/dl) | 14.6 ± 2.8 | 9.0 ± 0.8 | p<0.05 |

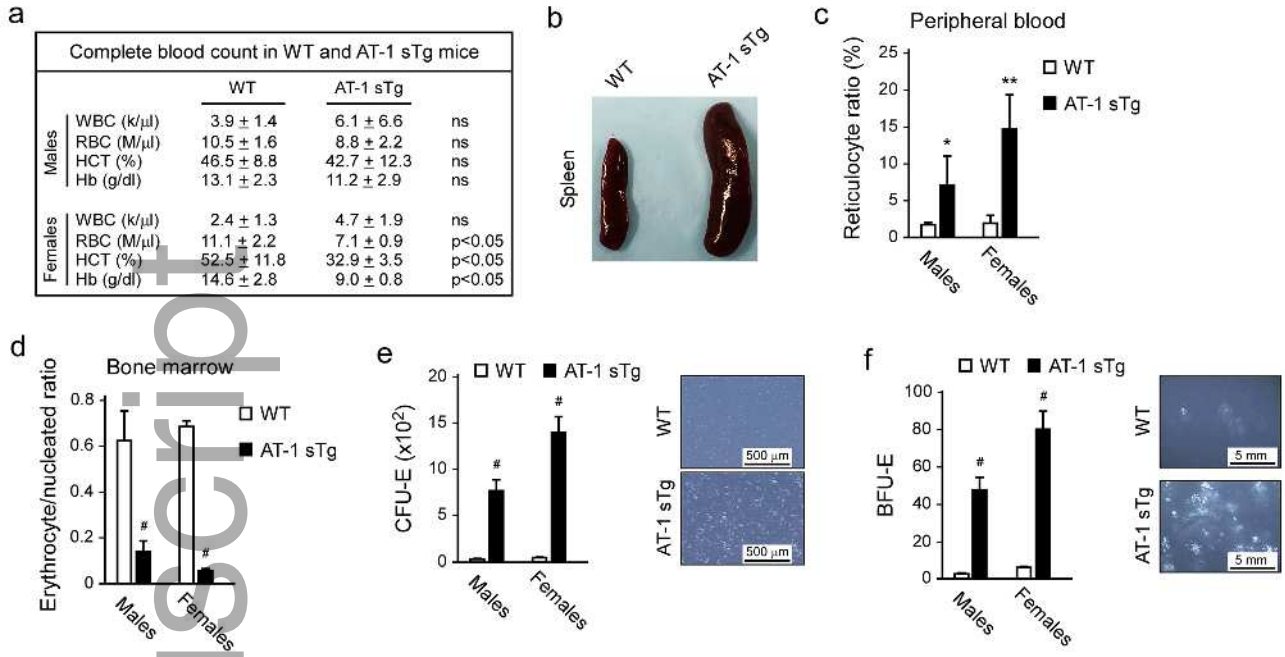


k

Plasma lipid profile in WT and AT-1 sTg mice

| | | Fed | | | Fasted | | |
|---|---|---|---|---|---|---|---|
| | | WT | AT-1 sTg | | WT | AT-1 sTg | |
| Males | Cholesterol (mg/dL) | 119.2 ± 19.3 | 60.6 ± 9.5 | p<0.0005 | 120.8 ± 9.1 | 70.8 ± 14.7 | p<0.0005 |
| | HDL (mg/dL) | 64.6 ± 7.2 | 30.0 ± 9.1 | p<0.0005 | 68.2 ± 3.5 | 29.0 ± 4.6 | p<0.0005 |
| | non-HDL (mg/dL) | 54.6 ± 12.3 | 30.6 ± 3.1 | p<0.005 | 52.6 ± 5.7 | 40.0 ± 9.5 | p<0.005 |
| | Triglycerides (mg/dL) | 72.2 ± 8.3 | 67.8 ± 21.3 | ns | 78.4 ± 7.9 | 69.0 ± 8.9 | ns |
| Females | Cholesterol (mg/dL) | 88.8 ± 12.5 | 62.2 ± 13.3 | p<0.05 | 90.8 ± 15.5 | 70.8 ± 14.7 | p<0.05 |
| | HDL (mg/dL) | 49.6 ± 5.0 | 33.0 ± 6.8 | p<0.005 | 46.2 ± 6.6 | 33.4 ± 10.5 | p<0.05 |
| | non-HDL (mg/dL) | 39.2 ± 9.1 | 28.2 ± 5.9 | p<0.05 | 44.6 ± 5.8 | 37.4 ± 4.8 | p<0.05 |
| | Triglycerides (mg/dL) | 67.8 ± 17.2 | 119.0 ± 29.7 | p<0.05 | 55.4 ± 7.2 | 59.2 ± 15.1 | ns |

acel_12820_f3.tif

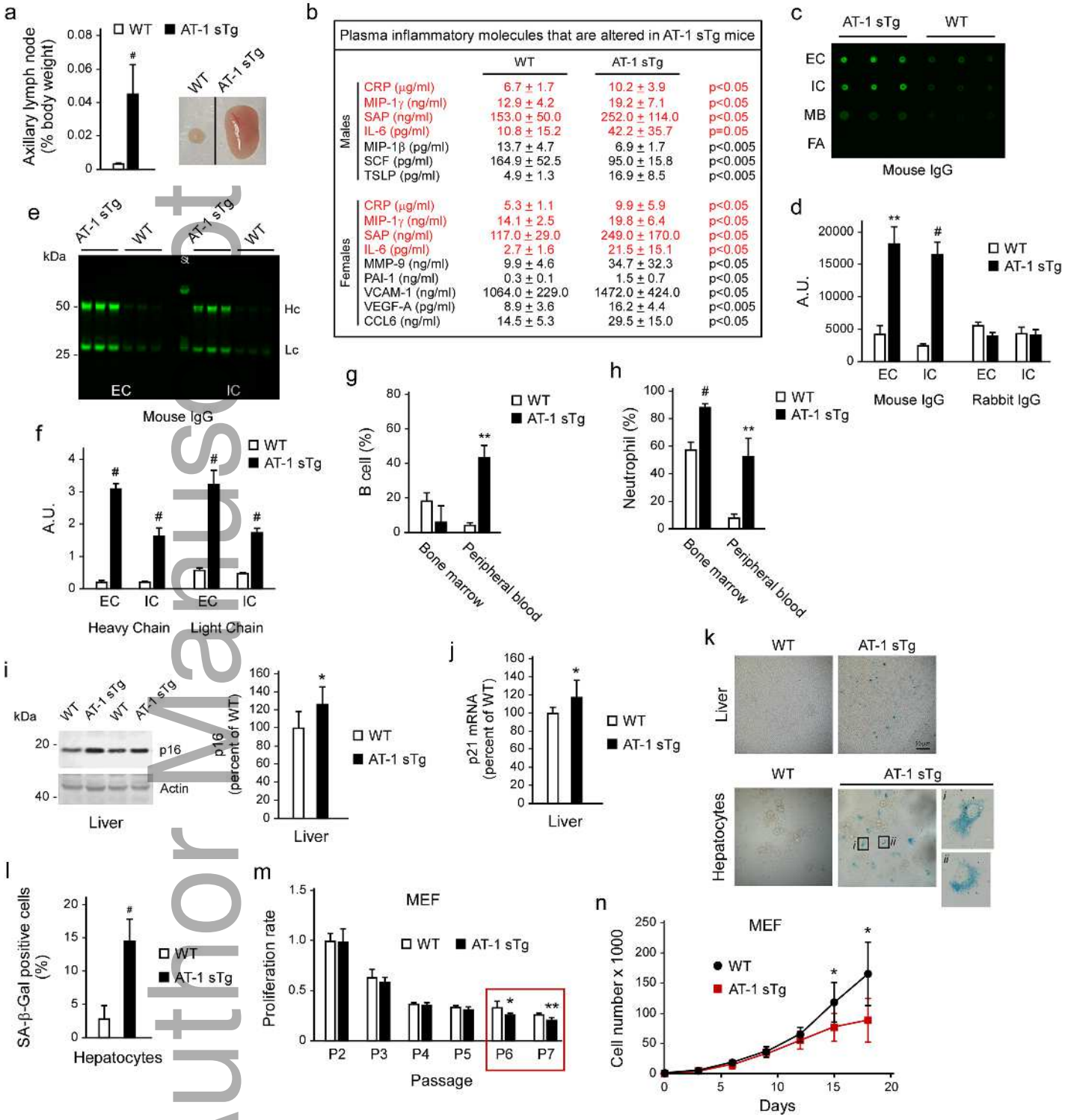


acel_12820_f4.tif

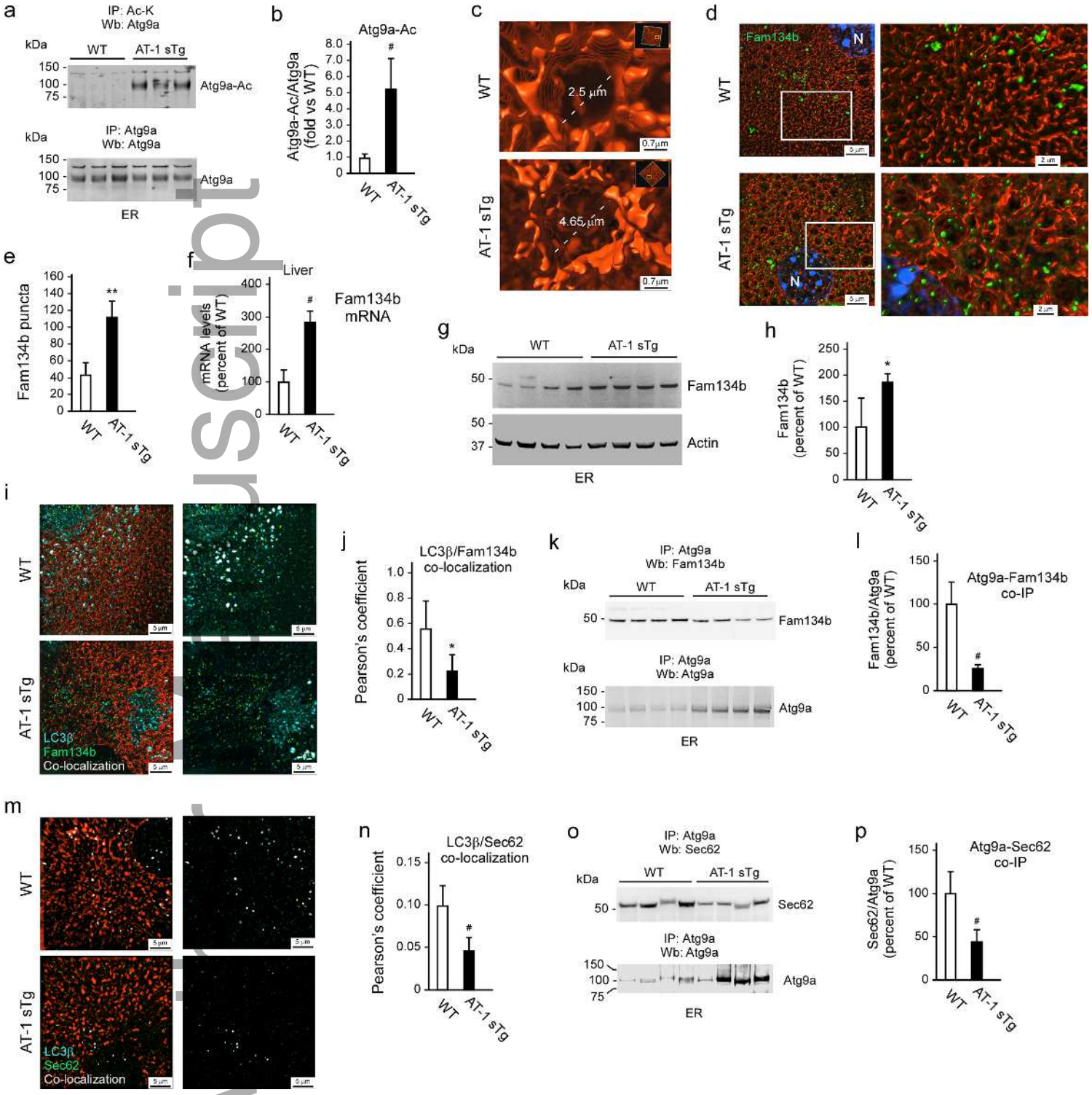


acel_12820_f5.tif

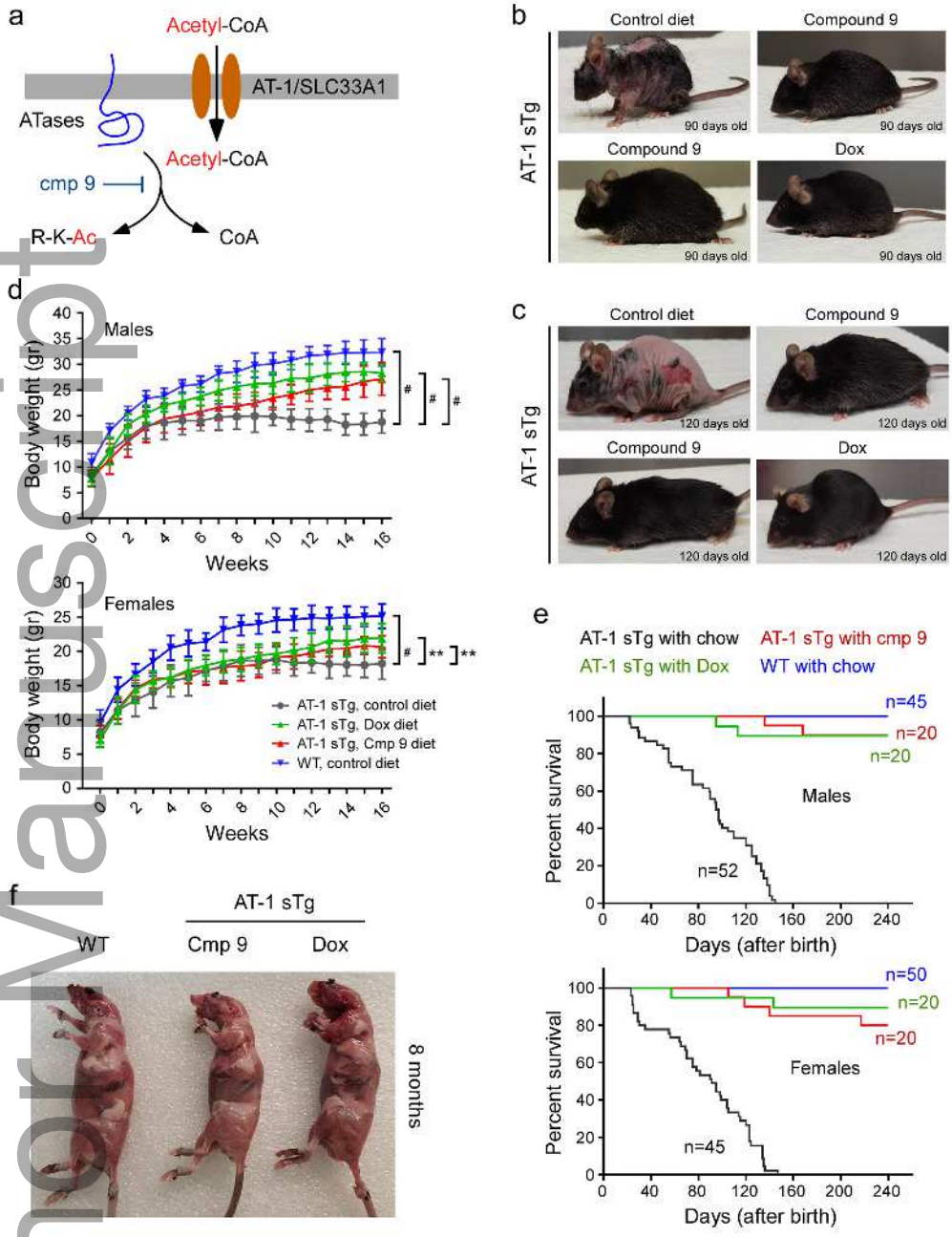


acel_12820_f6.tif

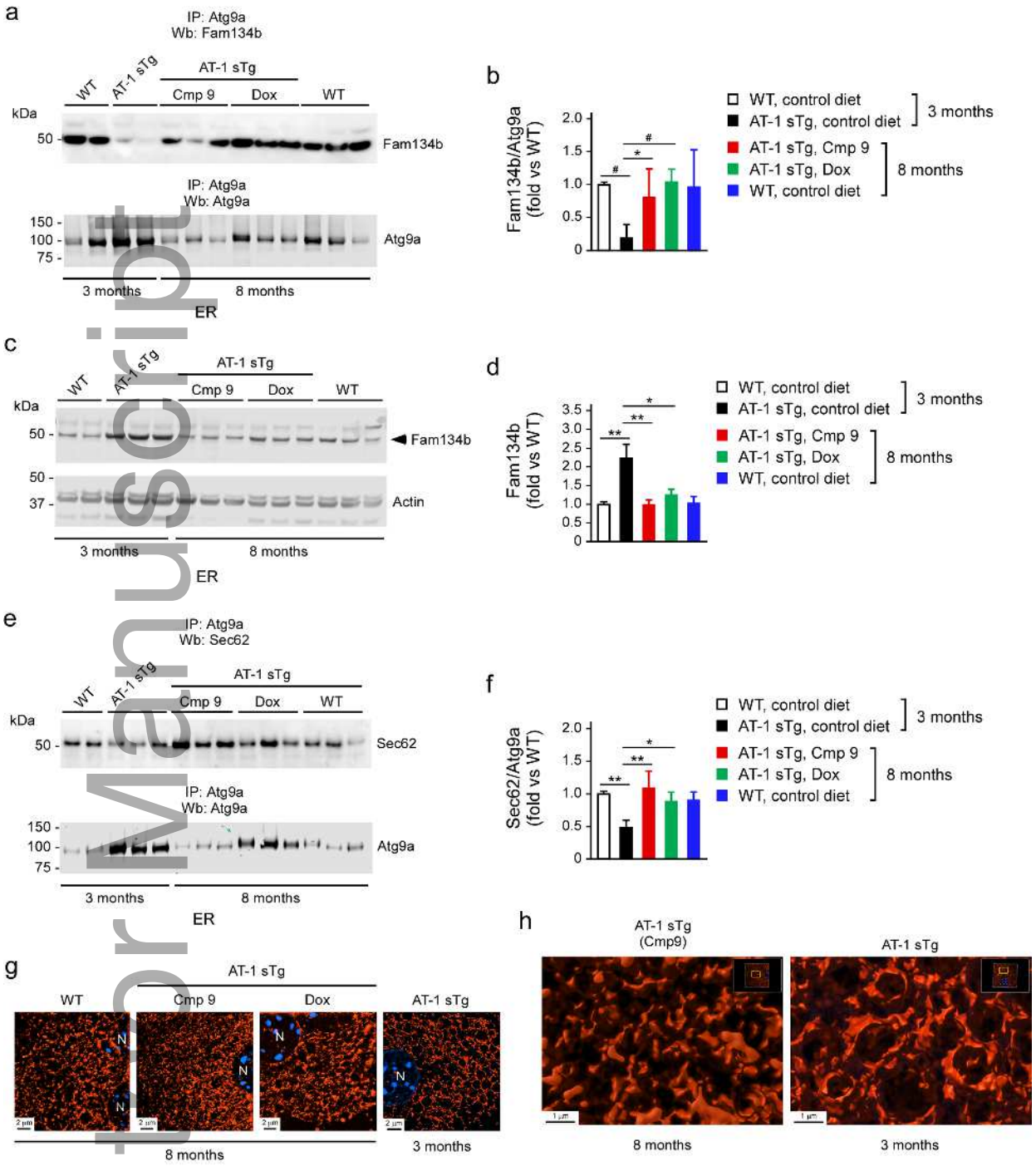


acel_12820_f7.tif